Additive Manufacturing 36 (2020) 101510

Contents lists available at ScienceDirect

Additive Manufacturing

journal homepage: www.elsevier.com/locate/addma

Full Length Article

Wire-arc additive manufactured nickel aluminum bronze with enhanced mechanical properties using heat treatments cycles

C. Dharmendra[a,*], B.S. Amirkhiz[a,b], A. Lloyd[c], G.D. Janaki Ram[a,d,1], M. Mohammadi[a]

[a] Marine Additive Manufacturing Centre of Excellence (MAMCE), University of New Brunswick, Fredericton, NB, E3B 5A1, Canada
[b] CanmetMATERIALS, Natural Resources Canada, 183 Longwood Road South, Hamilton, ON, L8P 0A5, Canada
[c] Department of Civil Engineering, University of New Brunswick, 17 Dineen Drive, Fredericton, NB, E3B 5A1, Canada
[d] Department of Materials Science and Metallurgical Engineering, Indian Institute of Technology Hyderabad, Kandi, 502285, Telangana, India

ARTICLE INFO

Keywords:
Nickel aluminum bronze (NAB)
Wire-arc additive manufacturing (WAAM)
Heat treatment
Electron microscopy
κ-Phases
Tensile properties

ABSTRACT

Wire-arc additive manufacturing (WAAM) technique was used to develop nickel aluminum bronze (NAB) components for naval applications. The microstructural changes were characterized using scanning electron microscopy (SEM) and transmission electron microscopy (TEM) with energy dispersive spectroscopy (EDS). As-built WAAM-NAB consists of κ_{II} (globular Fe_3Al) and κ_{III} (lamellar NiAl) phases in the interdendritic regions and fine Fe-rich κ_{IV} particles in the Cu-matrix. Along the build direction, the WAAM-NAB flat samples exhibited yield and ultimate tensile strength values of 380 and 708 MPa, respectively, and 34 % elongation. Furthermore, three different heat-treatments were performed on the samples in a view to evaluating their effect on mechanical properties. When heat-treated to 350 °C for 2 h (HT-1), there are no significant microstructural changes, and tensile properties along the build direction are similar to the as-built WAAM-NAB. Heat-treatment at 550 °C for 4 h (HT-2) produced a new needle-like κ_v phase in the α-matrix, coarsening of globular κ_{II}, partial spheroidization of lamellar κ_{III}, and reduced amount of κ_{IV} precipitation. As compared to the WAAM-NAB, HT-2 samples exhibited a significant increase in yield strength (~90 MPa), and ultimate tensile strength (~60 MPa); however, tensile ductility was observed to drop by 20 %. After heat-treatment at 675 °C for 6 h (HT-3), globular κ_{II} and needle-like κ_v were coarsened, lamellar κ_{III} was completely spheroidized, and the amount of κ_{IV} was significantly reduced. HT-3 samples showed better tensile strength (~37 MPa) than the WAAM-NAB with marginal loss (6%) in the ductility.

1. Introduction

Additive Manufacturing (AM) is evolving as a revolutionary tool and a disruptive technology in the 21st century. In addition to the aerospace and medical industries, AM can provide unique benefits to the shipbuilding and marine and offshore sectors as well [1–5]. Nickel Aluminum bronze (NAB) is a binary Copper-Aluminum alloy with additions of nickel, iron, and manganese. NAB alloys are widely in use in marine applications such as ship propeller, under-water fasteners, pumps, and valves, due to their excellent resistance to all forms of corrosion and erosion, high strength and toughness, and good damping capacity [6–11]. Solidification in alloy C95800 (Cu-9Al-4Fe-4Ni-1 Mn) primarily occurs by the formation of α-dendrites. The alloy undergoes a martensitic transformation if cooled quickly from elevated temperatures. The equilibrium phase diagram of this alloy is rather complicated with several possible microstructural phases, mainly κ-phases that absorb aluminum from the matrix (based on Fe_3Al or NiAl) [9,10]. Various κ-phases appear in the microstructure as the temperature falls during cooling (κ_I at ~1040 °C, κ_{II} at ~930 °C, κ_{III} at ~800 °C, κ_{IV} during further cooling if the cooling rate is slow).

In a recent publication [12], the present authors have reported a detailed study on the microstructural characteristics and tensile properties of wire-arc additive manufactured (WAAM) nickel aluminum bronze (Cu-9Al-4Fe-4Ni-1 Mn). The WAAM-NAB was found to exhibit many desirable microstructural features in comparison with the conventionally sand-cast samples. The WAAM-NAB exhibited a significantly finer α-dendritic structure without any rosette-like κ_I intermetallic particles. In the WAAM-NAB, the interdendritic regions contained some globular κ_{II} and lamellar κ_{III} intermetallic phases, but they were found to be relatively finer and fewer than in the cast-NAB.

* Corresponding author.
E-mail address: dharmendra.chalasani@unb.ca (C. Dharmendra).
[1] Dr. G.D. Janaki Ram was a Visiting Professor at the University of New Brunswick in Fredericton, New Brunswick, Canada during the completion of this work. He was formerly with the Department of Metallurgical and Materials Engineering, Indian Institute of Technology Madras, Chennai, 600036, India.

https://doi.org/10.1016/j.addma.2020.101510
Received 30 May 2020; Received in revised form 17 July 2020; Accepted 2 August 2020
Available online 09 August 2020
2214-8604/ Crown Copyright © 2020 Published by Elsevier B.V. All rights reserved.

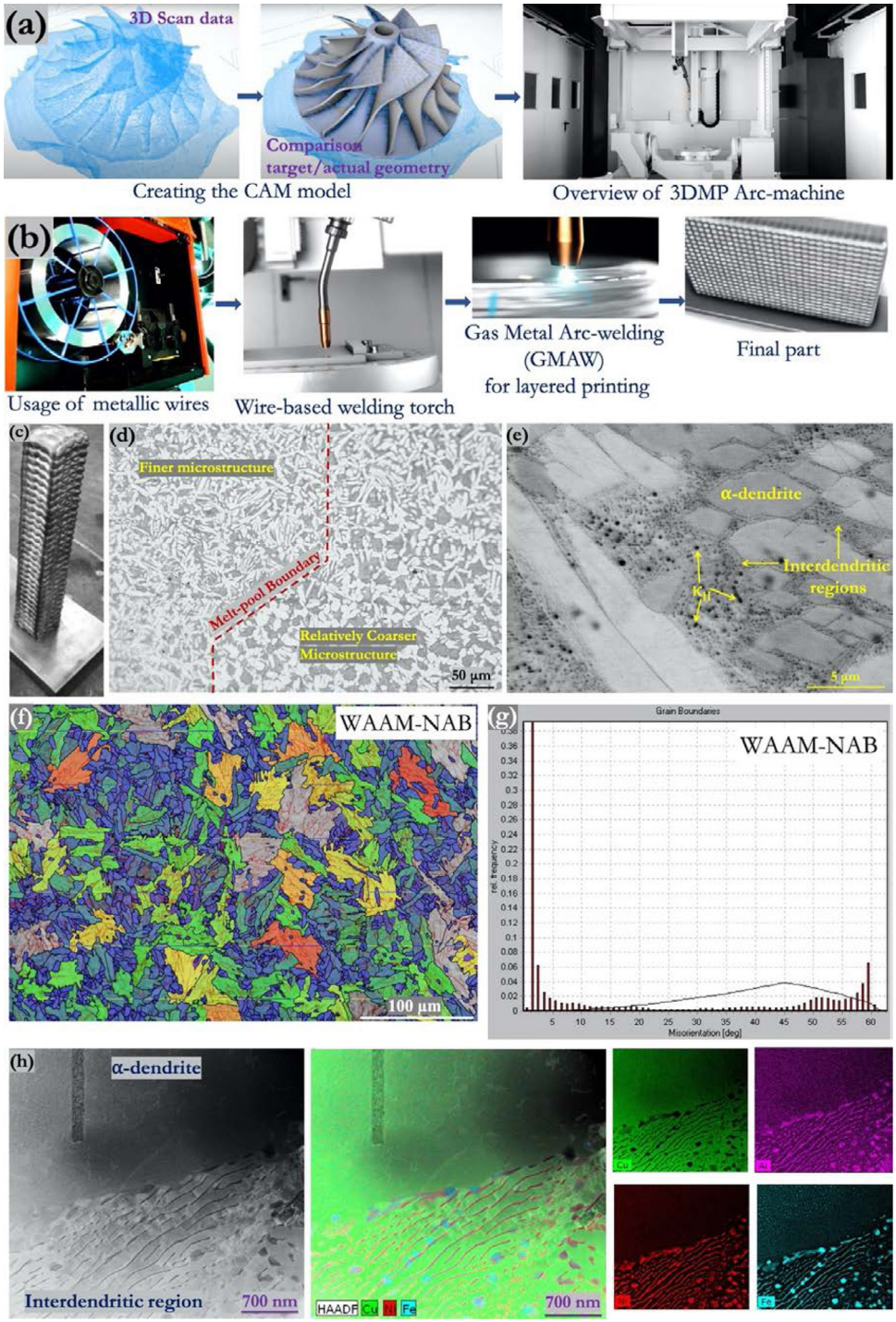

Fig. 1. (a and b) shows the steps involved in the Gefertec's 3DMP wire-arc additive manufacturing (WAAM) process, (c) photograph of nickel aluminum bronze (NAB) square bar printed on a 316 L stainless steel substrate, (d) optical and (e) backscattered electron SEM micrograph of WAAM-NAB sample, (f) EBSD image of WAAM-NAB and (g) the corresponding misorientation distribution, and (h) STEM-HAADF image and the EDS elemental maps of Cu, Al, Ni, and Fe.

Importantly, the WAAM-NAB showed extremely fine (5 − 10 nm) homogeneously precipitated κ_{IV} precipitates in the α-matrix. In comparison, the cast-NAB showed much coarser and fewer κ_{IV} precipitates. These unique microstructural features in the WAAM-NAB have led to substantially higher strength as well as tensile ductility as compared to the cast samples. It has been reported that, in the case of selective laser melted (SLM)-NAB, martensitic β-phase forms, which exhibits less tensile ductility and is also more prone to preferential corrosion [13]. Another beneficial feature of WAAM-NAB is the absence of martensitic β-phase in the microstructure in the as-built condition.

While the as-fabricated WAAM-NAB parts can achieve superior tensile properties as compared to conventional sand-casting NAB parts, it may be possible to further enhance their mechanical properties by employing an appropriate post-processing heat treatment. In this regard, in the first place, it is appropriate to consider the heat-treatments commonly used for NAB castings and welds. It is not uncommon to use NAB castings in the as-cast condition. However, for achieving the best corrosion performance in NAB castings, heat-treatment at 675 °C for 6 h is often specified [10,14–19]. This heat-treatment is meant to spheroidize the lamellar κ_{III} precipitates, which would otherwise provide a

Table 1
Process parameters for wire-arc deposition of NAB on 316L stainless steel substrate.

Current	Voltage	Travel speed	Wire feed rate	Heat input
114 Amp	12.5 V	480 mm/min	6.5 m/min	170 J/mm

large surface area for micro-galvanic coupling leading to inferior corrosion resistance. In the case of fusion welds, such post-weld heat treatment is rarely feasible or used, but a stress-relieving treatment in the range of 300 − 400 °C is done wherever possible for improving stress corrosion cracking resistance [20]. Typically, heat-treatment of cast-NAB at temperatures less than 800 °C does not cause for any changes in the primary phases, except the transformation of any retained β to α + κ. However, there is a significant increase in the volume fraction of the fine κ_{IV} precipitates, as in the case of heat-treatment at 675 °C for 6 h [10,16].

The optimum heat-treatment for WAAM-NAB parts can be expected to be different from that of conventional sand-castings given the substantial differences in the starting microstructures. For example, depending on the heat-treatment temperature, there can be significant fresh precipitation of κ-phases in the WAAM-NAB, which may significantly influence both mechanical properties and corrosion performance. This is usually not the case in castings because of the prolonged cooling rates; precipitation of the κ-phases occurs to the fullest extent during casting itself. Further, the lamellar κ_{III} phases in WAAM-NAB may spheroidize at a lower temperature and/or in a shorter time as the fast cooling rates in WAAM processing result in the formation of finer and thinner κ_{III} lamellae than in conventional cast processing. Hence, apart from the standard heat-treatment at 675 °C commonly used for NAB castings and stress-relieving treatment at 350 °C, generally employed for NAB fusion welds, it is prudent to consider an additional heat treatment at around 550 °C for WAAM-NAB. The implications of any post-processing heat treatments for WAAM-NAB must be considered not only on the mechanical properties but also on corrosion behavior.

Available information on heat-treatment of WAAM-NAB parts is minimal [21,22]. In a recent study by Chen Shen et al. [21], tempering of WAAM-NAB samples was attempted in the temperature range of 450 °C–750 °C for 6 h after a homogenization treatment at 900 °C for 2 h followed by water quenching. The best tensile properties were reported

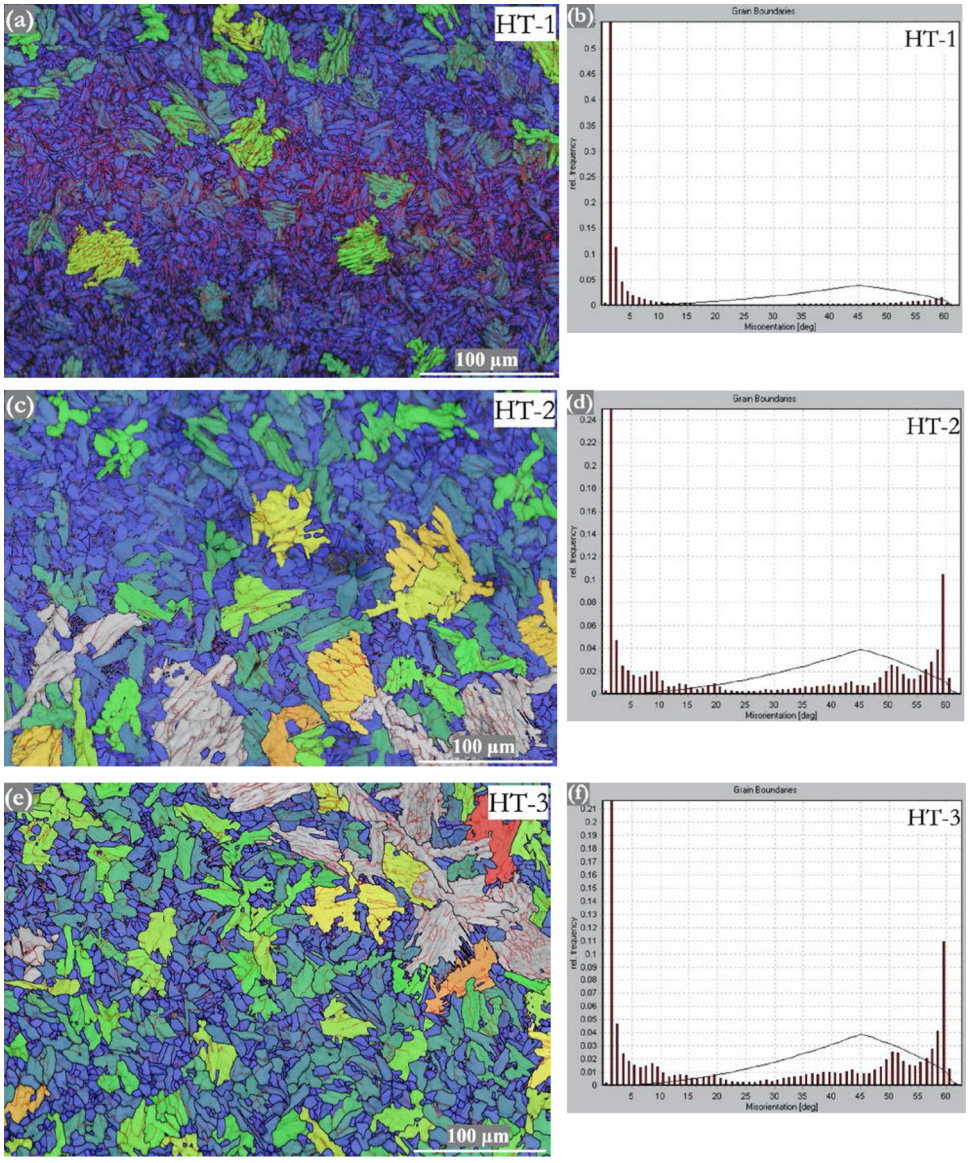

Fig. 2. EBSD images of WAAM-NAB in (a) HT-1, (c), HT-2, and (e) HT-3 conditions and the corresponding misorientation distribution are shown in (b), (d), and (f), respectively.

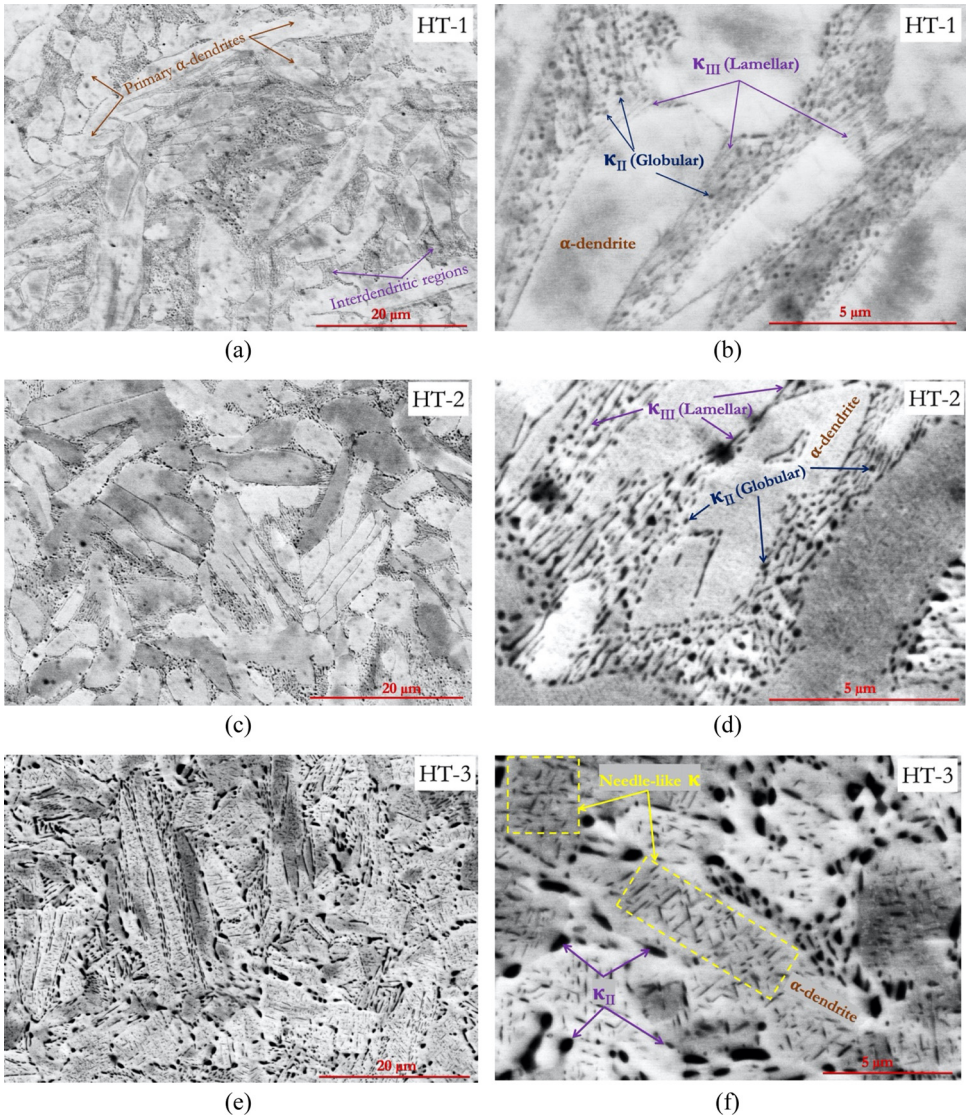

Fig. 3. SEM-Backscattered electron images of (a and b): HT-1, (c and. D): HT-2, and (e and f): HT-3 samples.

in samples tempered at 650 °C for 6 h. An increase in the tempering temperature to 750 °C was found to affect the tensile performance significantly. In a follow-up investigation, Chen Shen et al. [22] further reported tensile properties of WAAM-NAB samples (in longitudinal orientation) after a direct tempering of as-fabricated WAAM-NAB samples at 675 °C for 6 h (no prior homogenization step was used in this case). The results showed that the use of a homogenization treatment at 900 °C has no particular beneficial effect on the final tensile properties of WAAM-NAB. The use of such very high-temperature heat treatments, especially those involving water quenching, have minimal applicability from a practical standpoint.

In the current work, WAAM-NAB samples have been heat-treated at 350 °C for 2 h, 550 °C for 4 h, and 675 °C for 6 h. Detailed microstructural characterization and tensile testing after the three different heat-treatments were carried out. Emphasis has been placed on understanding the evolution of various κ-phase precipitates as a function of heat-treatment conditions and establishing the structure-property relationships in heat-treated WAAM-NAB.

2. Experimental work

2.1. Material and heat-treatment

Nickel aluminum bronze (Cu-9Al-4Ni-4Fe-1 Mn) square bars of 25 mm × 25 mm × 160 mm (length × width × height), vertically built on a commercial wire-arc additive manufacturing machine (GEFERTEC's arc 605), were used to conduct experimental studies in this investigation. Fig. 1(a) and (b) present the steps involved in the 3DMP (3D metal printing) process, which uses metallic wires and Gas Metal Arc Welding (GMAW) technology. The CAM (computer-aided manufacturing) software converts the data into sliced up individual digital layers and offer the layered printing in a fully automated and digitally controlled manner. The primary processing conditions used to deposit NAB square bars on 316L stainless steel substrate are listed in Table 1. These parameters were selected based on optimization trials for visible defect-free parts.

Fig. 1(c) shows the bulk NAB alloy square bar printed via the WAAM process. The samples for heat-treatment were cut along the building direction and subjected to three different heat-treatments, (i) 350 °C/2 h (hereafter, denoted as HT-1), (ii) 550 °C/4 h (hereafter, denoted as HT-2), and (iii) 675 °C/6 h (hereafter, denoted as HT-3). In all the cases, samples were subsequently furnace cooled.

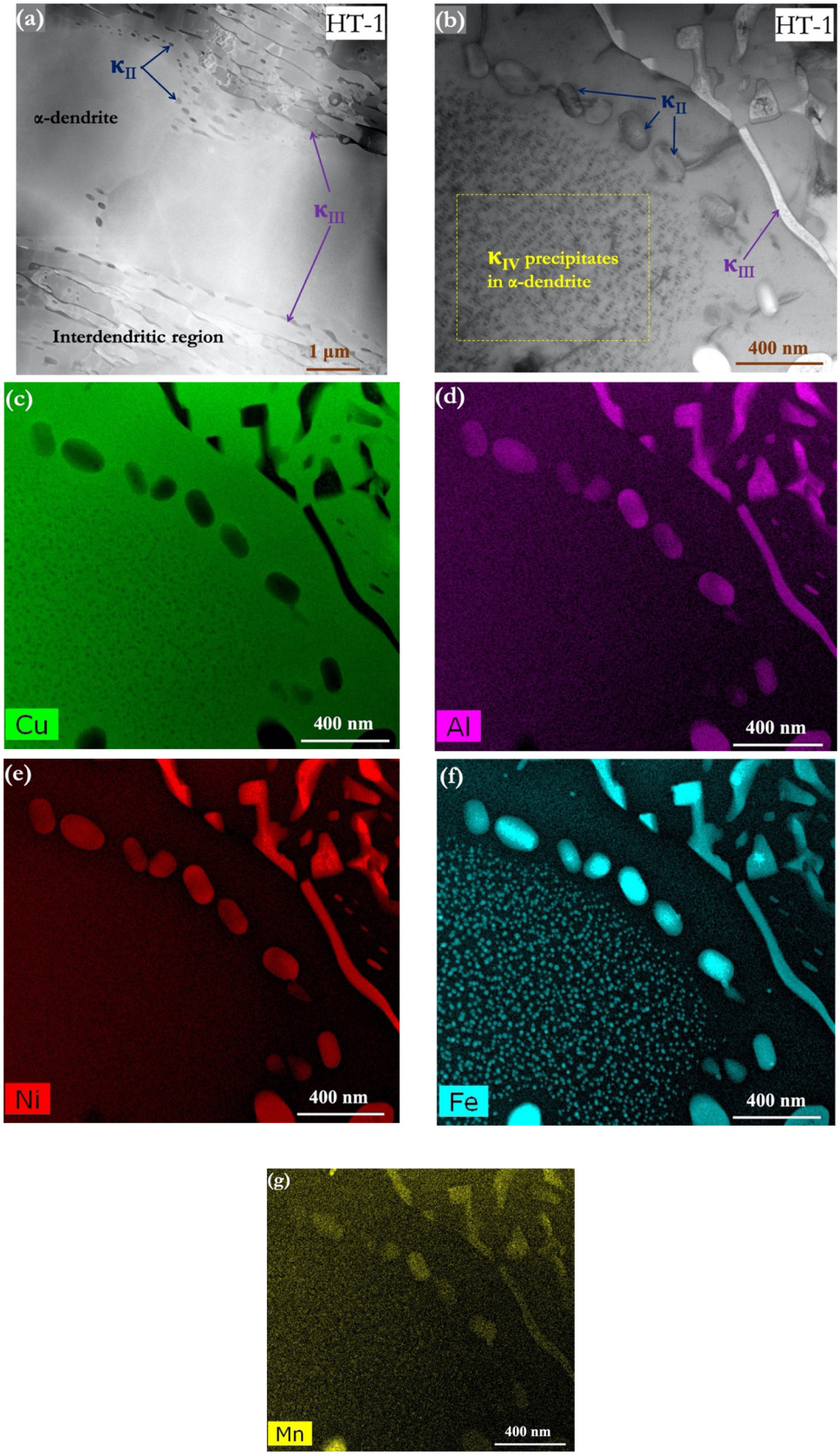

Fig. 4. (a) STEM-HAADF and (b) STEM-Bright field (BF) images of HT-1 sample at low and high magnifications, respectively. (c) to (g) show the EDS elemental maps of Cu, Al, Ni, Fe, and Mn, respectively, corresponding to the image shown in (b).

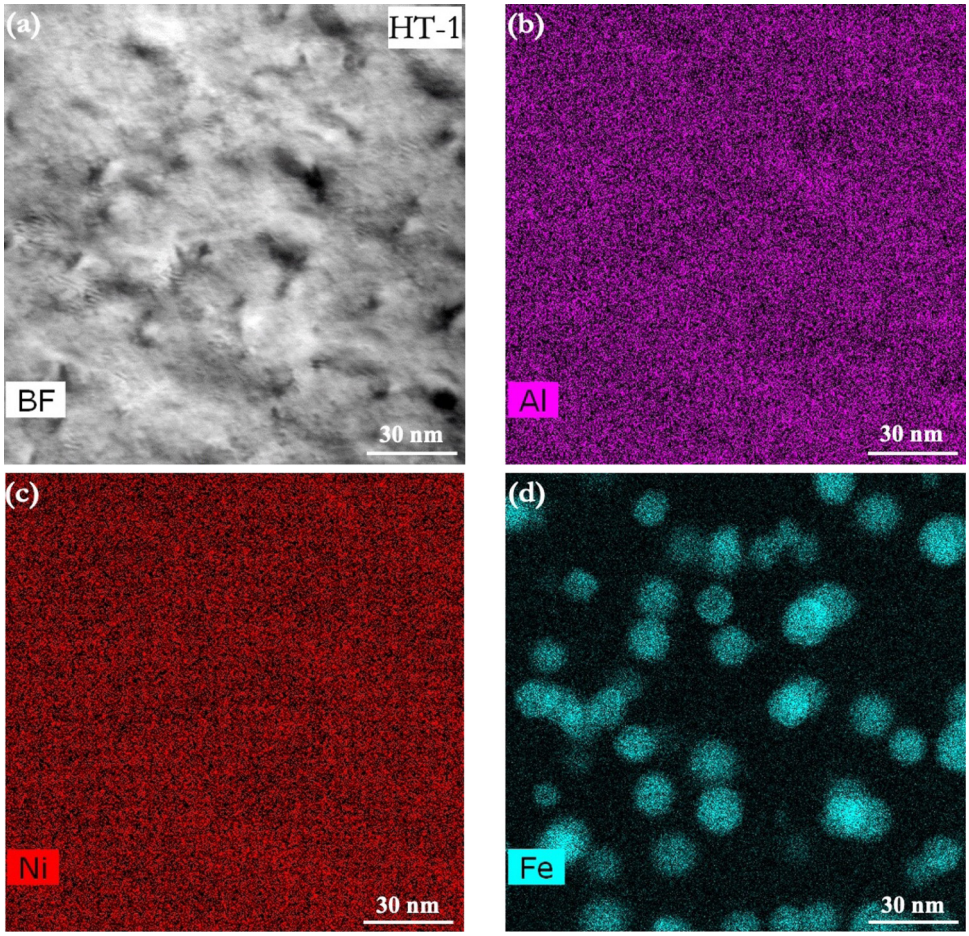

Fig. 5. (a) STEM-BF image of HT-1 sample in the α-matrix region; (b)-(d) show corresponding EDS elemental maps for Al, Ni, and Fe, respectively. Fe-precipitates (κ_{IV}) is in size of ~10 nm. Note that the thickness of TEM thin foil is ~100 nm.

2.2. Microstructural characterization

The samples of HT-NAB for metallography were cut from the plane parallel to the building direction and were mounted, polished, and etched with Klemm's reagent. The microstructures of the heat-treated samples were examined using the Zeta-20 optical microscope, and FEI's Scios 2 focused ion beam (FIB)-scanning electron microscope (SEM). For transmission electron microscope (TEM) characterization, heat-treated samples were mechanically polished to a thickness of 30 μm. A Gatan Precision Ion Polishing System (Gatan model 695) was used for further thinning through the ion-beam milling technique using liquid nitrogen cooling at 5,3, and 1 keV and a gun angle of 4° for 130, 10 and 30 min average time at each step, respectively. FEI Tecnai Osiris TEM equipped with a 200 keV X-FEG gun was used for microstructural studies. High angle annular dark-field (HAADF) detectors were used in combination with Energy Dispersive Spectroscopy (EDS) to obtain elemental distribution maps, where a sub-nanometer electron probe was used to obtain spatial resolutions in the order of 1 nm. Electron diffraction techniques were used to obtain crystallographic information from the matrix and the intermetallic particles. Electron backscatter diffraction (EBSD) analysis was performed on HT-NAB samples on a plane parallel to the build direction using FEI's Scios 2 SEM system at 20 KV through an integrated Oxford/HKL EBSD detector (Oxford EBSD-Integrated AZtecHKL system automated with Symmetry). The raw data was post-processed using the Channel 5 software.

2.3. Tensile testing

Mechanical properties of all heat-treated NAB samples were evaluated at room temperature under quasi-static uniaxial tensile loading. Tensile testing was conducted on sub-size flat specimens as per the ASTM E-8 standard [23], where tensile axes were parallel to the build direction. The dimensions were 60 mm total length, 12 mm parallel length, 10 mm gauge length, 3 mm gauge width, 6 mm fillet radius, and 2 mm thickness. A computer-controlled Instron model 1332 universal testing machine that was accompanied by a 25 mm Instron extensometer (for accurate measurements of displacement) was used to perform the tensile tests. Samples were tested until failure at a constant crosshead displacement rate (0.005 mm/min), and the data for engineering stress were simultaneously recorded during the testing. Tensile tests were performed on multiple (3–5) samples to confirm the repeatability of the results, where a typical tensile engineering stress-strain curve was plotted. Fracture surfaces of tensile tested specimens were characterized using *FEI's Scios 2* SEM.

Digital Image Correlation (DIC) technique was also used to determine the displacement and subsequent calculation of tensor components of local strain fields during tensile deformation. As the tensile specimens were flat (planar), the DIC system used a single 5 M P global shutter CMOS sensor camera for in-situ images recording and to measure the 2D surface strain fields on the specimens. The camera was aligned at 90° to the specimen's plane and vertically at 100 mm away from the specimen. The image capturing system recorded 1000–4000 frames at an interval of 2 s. Although all the specimens were tested to failure with the same strain rate, the total number of frames collected varied due to the difference in the strain exhibited by different test samples. High contrast speckle patterns were applied to the surface of the tensile samples before testing to facilitate the pattern recognition analysis in the image correlation.

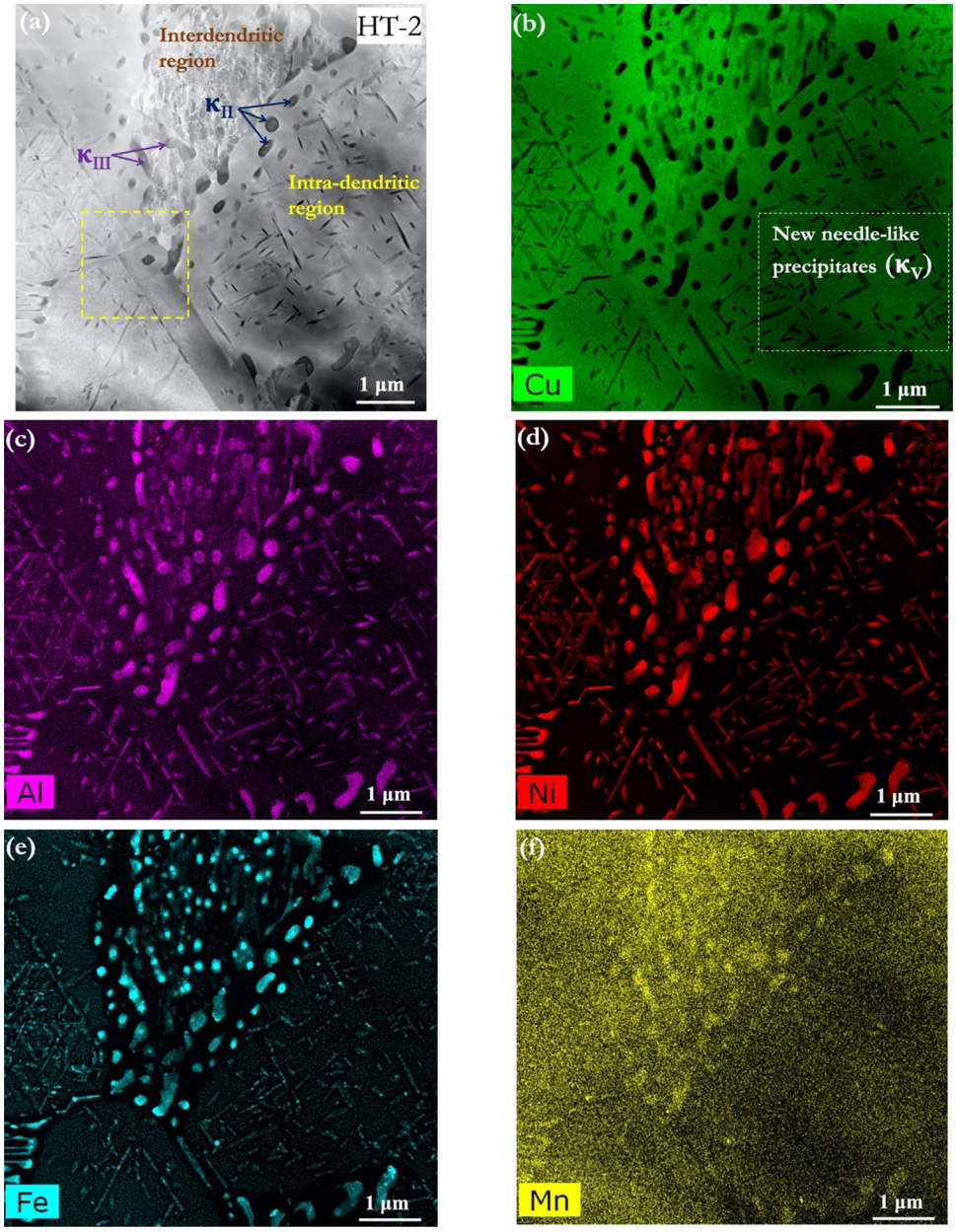

Fig. 6. (a) STEM-HAADF image of HT-2 sample showing both interdendritic and intra-dendritic regions, (b)-(f) show the corresponding EDS elemental maps of Cu, Al, Ni, Fe, and Mn, respectively. Note intra-dendritic needle-like intermetallic precipitation (κ_V) containing Ni, Al, and some Fe.

Table 2
Chemical analysis of κ_V precipitates within the α-matrix of HT-2 and HT-3 samples.

κ_v Phase	Elements in wt. % from STEM foil			
	Cu	Al	Ni	Fe
HT-2	18.1 ± 1	18.8 ± 2	49.6 ± 4	13.3 ± 2
HT-3	18.7 ± 0.3	19.7 ± 0.2	40.3 ± 0.8	21.2 ± 0.25

3. Results

3.1. Microstructures of as-built and heat-treated WAAM-NAB

Multiples of macro-view images were used to estimate the amount of porosity on plane parallel and perpendicular to the build direction. It was observed that the deposited NAB is fully-dense without any apparent porosity, cracks, or fusion defects [12,24]. Fig. 1(d) shows the microstructure of WAAM-NAB near a melt pool boundary. The microstructure below the melt pool boundary is relatively coarser. Primary α-dendrites are brighter (whitish), and interdendritic regions are darker (blackish) in the micrograph. Only the SEM image (Fig. 1(e)) revealed some intermetallic particles (κ_{II}) in the interdendritic regions. Fig. 1(f) and (g) presents the EBSD grain boundary distribution map and corresponding grain-to-grain misorientation angle distribution (in the α-matrix) histogram, respectively. The grain size (~8 μm) was measured using a linear intercept method. TEM characterization of the WAAM-NAB sample revealed the presence of globular κ_{II} (Fe_3Al) and lamellar κ_{III} (NiAl) in the interdendritic regions and uniform distribution of Fe-rich fine κ_{IV} precipitates (5–10 nm) in the α-matrix. It may be noted that, unlike in the cast-NAB, the κ_I intermetallic phase was not formed in the WAAM-NAB [12].

Fig. 2(a–f) shows EBSD grain boundary distribution maps and corresponding histograms representing grain-to-grain misorientation angle

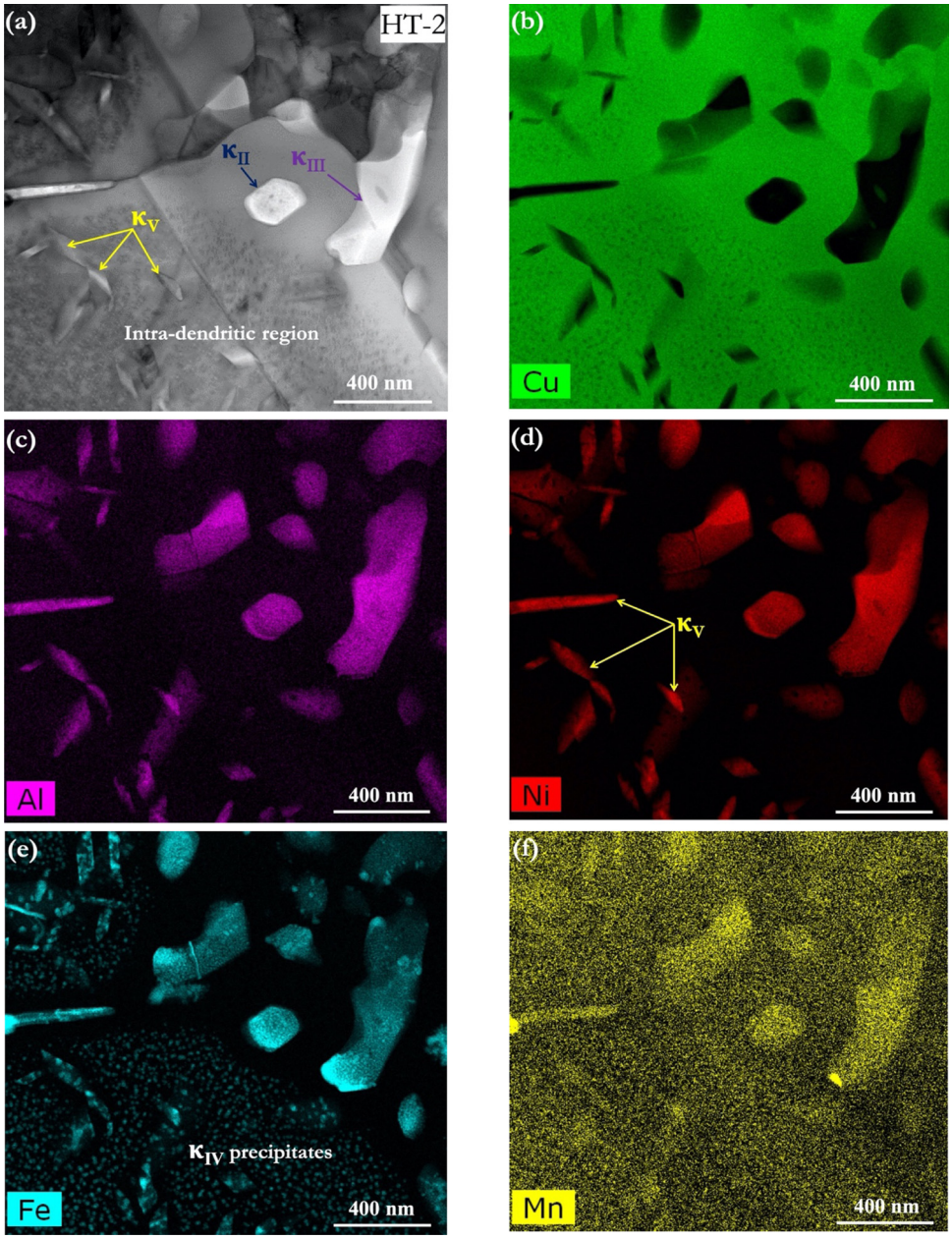

Fig. 7. (a) STEM-BF image and (b)-(f) show corresponding EDS elemental maps of Cu, Al, Ni, Fe, and Mn, respectively, of the boxed region shown in Fig. 5 for the HT-2 sample. Note very fine globular Fe-rich κ_{IV} precipitates in the α-matrix.

distribution (in the α-matrix) of all the heat-treated samples. As compared to WAAM-NAB, no significant differences in the size of α-dendrites/grains (~8 μm) were noticed after HT-1, and the dendritic structure remained intact. The grain size slightly increased to ~13 μm in HT-2 and HT-3 conditions, and the formation of equiaxed structure was evident after HT-3. Red lines in the grain boundary maps indicate the presence of low angle grain boundaries (LAGBs). Misorientation angle distribution plots for all the conditions obtained from the EBSD data (black line in the images correspond to the McKenzie plot for random distribution) reveals a difference in the population of the LAGBs. The peak in the misorientation angle distribution plot for the WAAM-NAB (Fig. 1(g)) shows the fraction of LAGBs (0–5 deg) as 39 %. The fraction of LAGBs increased to 55 % in the HT-1 condition, followed by a drop to ~22 and 25 % in HT-2 and HT-3 conditions. While LAGBs still account for the majority, the misorientation angle distribution is more uniform in HT-1, which may be attributed to microstructure recovery and substantial formation of subgrain boundaries. Formation of high angle boundaries (Fig. 1(e) and (g)) in HT-2 and HT-3 conditions is the result of an increase in the grain size and the associated grain boundary migration. Most of the misorientation angles of α-grains in HT-2 and HT-3 samples showed a 60° peak indicating the formation of new grains at an ideal misorientation angle for annealed twins (i.e., first-order twin relationship 60°/ < 111 > in face-centered cubic metals [25]).

As shown in Fig. 3(a) and (b), SEM examination of HT-1 samples did not reveal any significant microstructural differences from the as-fabricated WAAM-NAB samples. TEM examination also did not reveal any fresh intermetallic precipitation or noticeable coarsening of the κ_{II} and κ_{III} intermetallic phases, as shown in Fig. 4. However, the κ_{IV} precipitates appeared slightly coarser as compared to the as-fabricated samples. TEM-EDS elemental mapping was done at high magnification (Fig. 5(a–c)) to reveal the κ_{IV} precipitates, and corresponding elemental maps for Al, Ni, and Fe are presented in Fig. 5(d–f), respectively. While the κ_{IV} precipitates are in the size range of 5–10 nm in the WAAM-NAB

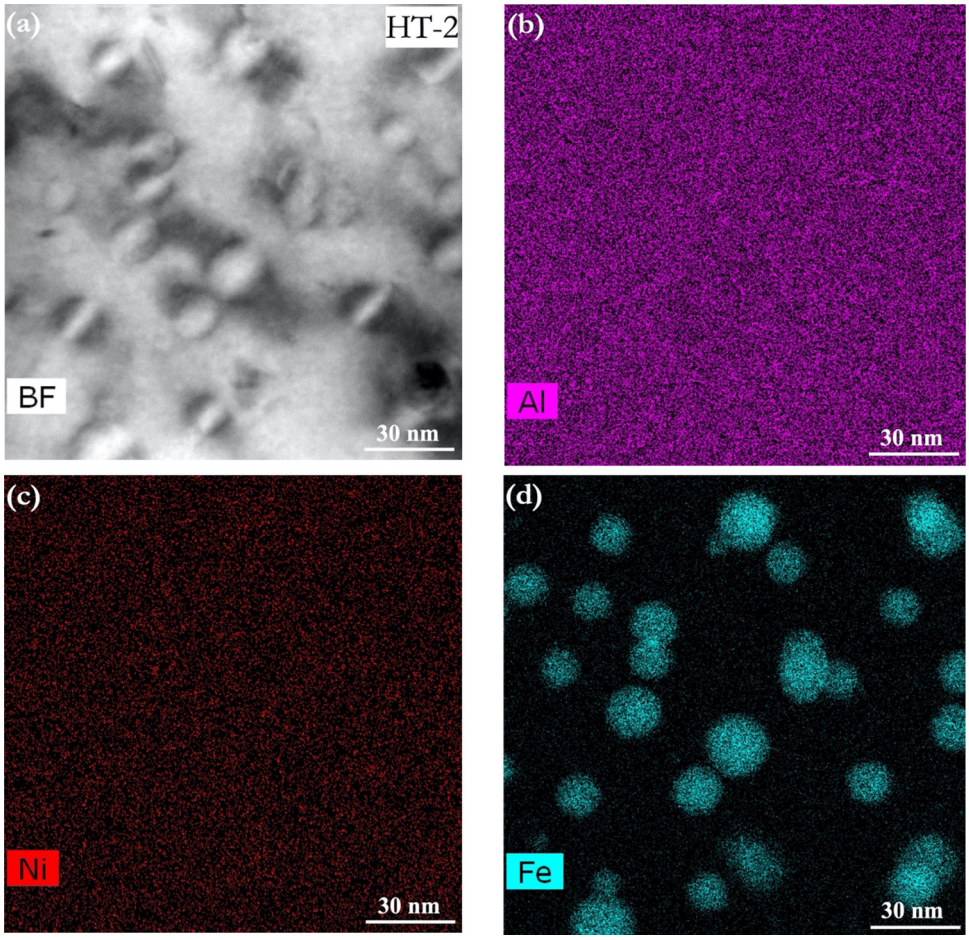

Fig. 8. (a) STEM-BF image of HT-2 sample in the α-matrix region; (b)-(d) show corresponding EDS elemental maps for Al, Ni, and Fe, respectively. Fe-precipitates (κ_{IV}) is in size of ~10 nm, and their precipitation is slightly lesser than in HT-1.

[12], the size of κ_{IV} precipitates in HT-1 samples appears to be close to 10 nm.

In contrast to HT-1, SEM examination of HT-2 samples (Fig. 3(c) and d)) showed perceivable coarsening of globular κ_{II} precipitates as well as a breakdown of lamellar κ_{III} phases into globular particles to some extent. Further, the HT-2 samples showed significant fresh precipitation of very fine needle-like phases in random orientations, which could only be revealed in the TEM examination (Fig. 6). These needle-like precipitates were found to contain Fe, Ni, and Al, as can be seen clearly in the EDS elemental maps. While these needle-like precipitates also correspond to the κ-phase (going by their chemical constitution), they cannot be identified under any of the four κ sub-classes (κ_I to κ_{IV}) as per convention [9,10,26–29] because of their distinctly different morphology. It is, therefore, prudent to identify these needle-like κ precipitates as a new sub-class – κ_v. Such needle-like κ-precipitation within the α-matrix has been reported earlier in cast nickel aluminum bronze after heat-treated at 675 °C [9,30]. Chemical analysis of the κ_v phase at multiple locations (Table 2) revealed that it is a nickel-rich aluminide with some amount of substitutional Fe (~13 wt.%). These findings are consistent with those reported by Hasan et al. [30] and Culpan and Rose [9], although the latter measured slightly higher Fe and Al contents (~27 wt.% each) in the κ_v phase. TEM examination of the HT-2 samples at higher magnifications (boxed area in Fig. 6a) further revealed the presence of very fine spherical κ_{IV} precipitates in the α-dendrites (Fig. 7). The κ_{IV} precipitation appeared to be relatively less in HT-2 samples than in as-fabricated and HT-1 samples. However, the size of κ_{IV} precipitates (shown in Fig. 8) appeared to be more or less the same in all the samples.

Compared to HT-2 samples, HT-3 samples revealed significantly coarser κ_{II} precipitates and an almost complete breakdown of lamellar κ_{III} into globular particles (Fig. 3(e) and (f)). Further, the HT-3 samples showed significantly coarser needle-like κ_v in the α-dendrites, which could be revealed even in the SEM examination. The composition analysis for the κ_v in the HT-3 condition (Table 2) showed a decline in Ni and an increase in Fe content. TEM examination (Fig. 9) confirmed the presence of κ_{IV} precipitates in HT-3 samples. In contrast to HT-1 and HT-2, HT-3 samples showed very few κ_{IV} precipitates, albeit with no significant difference in their size (Fig. 10).

The needle-like κ_v precipitates that were formed in the α-matrix (copper) were shown in Figs. 11(a) and (c). This intermetallic phase was found to be NiAl, based on the diffraction pattern analysis shown in Fig. 11(d). Fig. 11(e) and (f) show typical high-resolution TEM (HRTEM) images of κ_v precipitates in the HT-2 and HT-3 samples along with fast Fourier transform (FFT) patterns corresponding to κ_v and α-matrix. FFT lattice patterns of matrix and κ_v indicate that there is an orientation relationship between the two; however, κ_v precipitates appear to exhibit semi-coherency with the α-matrix in both HT-2 and HT-3 conditions as indicated by the presence of misfit dislocations at the interface. Similar to lamellar κ_{III}, κ_v particles are also NiAl that belong to B2 (ordered BCC) crystal structure [30]. In the ref [9], two types of morphologies (needle-liked and ovate-shaped) for κ_v were reported and hypothesized that the needle-like particles are nucleated in the α-matrix while oval-shaped precipitates nucleated epitaxially on pre-existing particles (i.e., finer κ_{IV} in the matrix). In the latter case, the composition at the central portion (Fe_3Al) of the κ_v particle was different from that of its extremities (NiAl), i.e., an equilibrium phase incorporating both

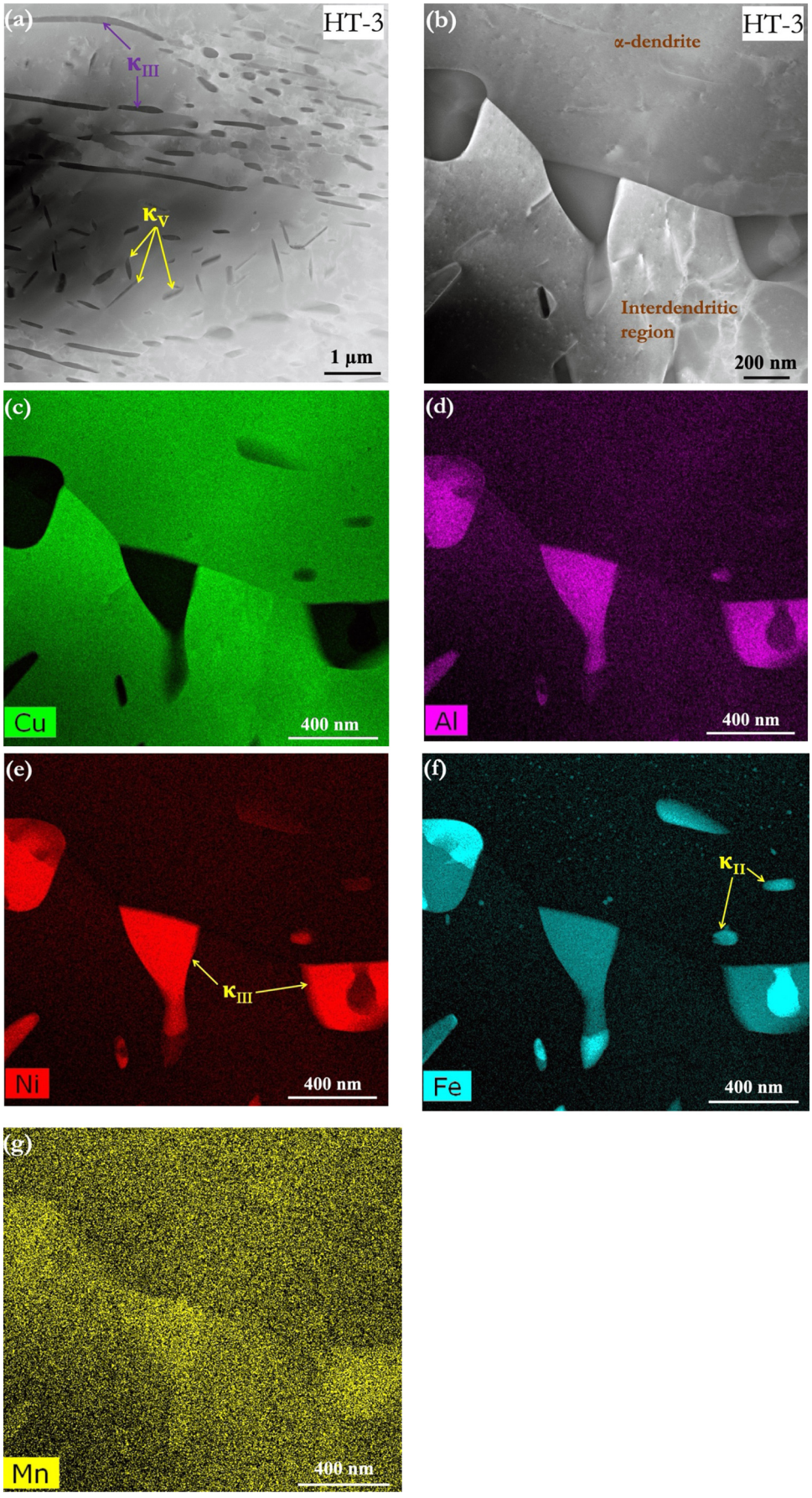

(caption on next page)

Fig. 9. (a) and (b) STEM-BF images of HT-3 sample at low and high magnifications, respectively. (c) to (g) show the EDS elemental maps of Cu, Al, Ni, Fe, and Mn, respectively, corresponding to the STEM-HAADF image shown in (b). Note coarser and fewer needle-like precipitates and less prominent κ_{IV} precipitation in the α-dendrites as compared to HT-2 condition.

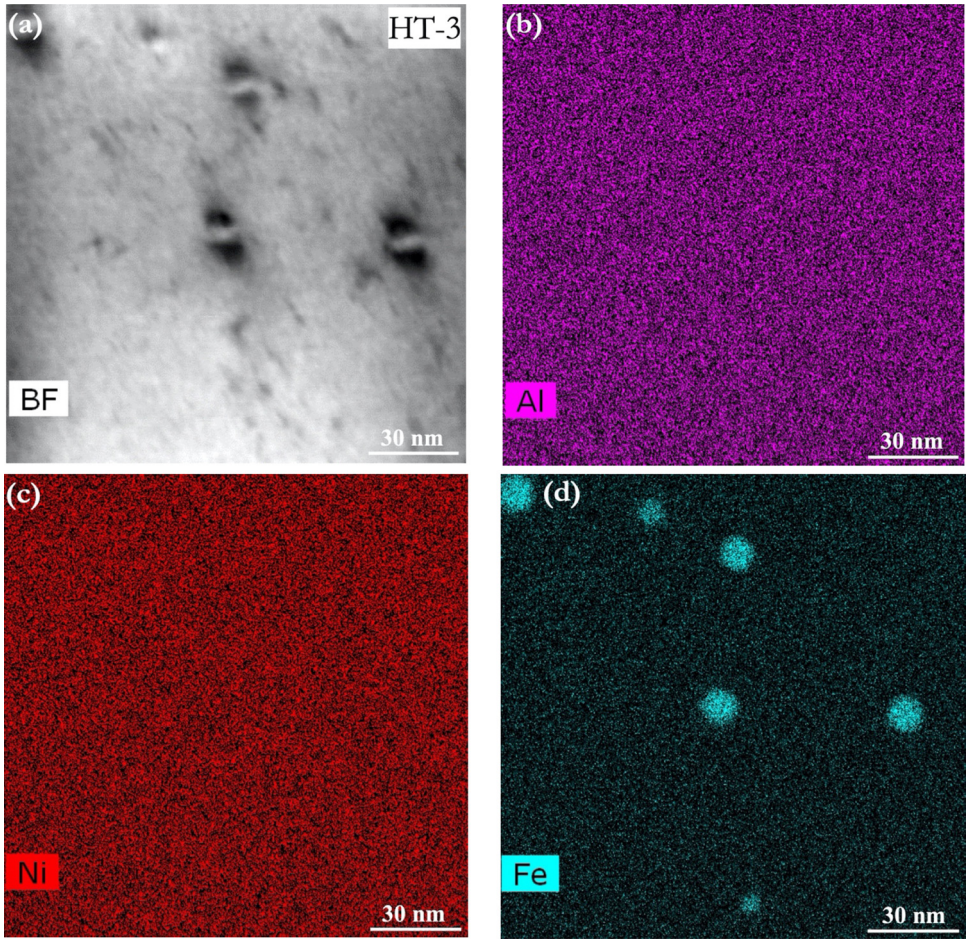

Fig. 10. (a) STEM-BF image of HT-3 sample in the α-matrix region; (b)-(d) show corresponding EDS elemental maps for Al, Ni, and Fe, respectively. Fe-precipitates (κ_{IV}) is in size of ~10 nm, and their precipitation is significantly lesser than in WAAM-NAB, HT-1, and HT-2 conditions.

Fe_3Al and NiAl compounds. It can be presumed in the present case that the κ_v particles are nucleated in the Cu-matrix as they are all in needle-like morphology.

3.2. Tensile properties of heat-treated NAB

Fig. 12 shows the typical tensile engineering stress – engineering strain plots of various heat-treated samples. A tensile plot of as-fabricated WAAM samples is included for easy comparison. The results of tensile testing are summarized in Table 3. As can be seen, HT-1 samples showed very similar tensile properties to as-fabricated WAAM samples. In contrast, HT-2 samples showed significantly higher yield and tensile strengths, but substantially lower ductility than as-fabricated samples. On the other hand, HT-3 samples showed a slight increase in yield and tensile strengths without much drop in tensile ductility when compared to as-fabricated samples.

Overall, HT-2 samples exhibited the highest strength among all the samples, while HT-3 samples showed the best combination of strength and ductility. Examination of tensile fracture surfaces of various heat-treated samples (Fig. 13) revealed predominantly dimpled rupture features in all the cases. However, some local regions of flat fracture features (shown by yellow arrows) corresponding to lamellar κ_{III} phases in the interdendritic regions are noticeable in HT-1 and HT-2 samples. Such regions were absent in HT-3 samples. Among all the fracture surfaces, HT-2 samples revealed less ductile fracture features.

Strain fields are generated from the DIC system software, which are shown for WAAM-NAB, HT-1, HT-2, and HT-3 specimens in Fig. 14(a–d), respectively. These strain fields are from the beginning of the test to the failure of the specimens. At fracture strain, the paint delaminated, resulting in the loss of strain field at the necking region. As per the appearance of the colors, the WAAM-NAB and HT-1 samples show regions of uniform strain distribution until the peak occurred in the center at fracture strain (~0.31). The strain fields for the HT-2 sample exhibited local strain concentrations (due to more pronounced precipitation of needle-like κ_v precipitates), while the strain behavior for HT-3 specimens seems to be more homogeneous. In WAAM-NAB, HT-1, and HT-3 specimens, the maximum strain and failure occurred at the center. On the other hand, the HT-2 specimens exhibited distinct strain variations (i.e., non-uniform distribution of plastic strain) along the gauge length and low tensile ductility.

4. Discussion

The results show that the heat treatment of WAAM-NAB samples at 350 °C for 2 h has not resulted in any significant microstructural changes from as-fabricated conditions. The slight coarsening of the κ_{IV} precipitates in HT-1 samples also seems to be insignificant. This is reflected in almost similar tensile properties of HT-1 and as-fabricated

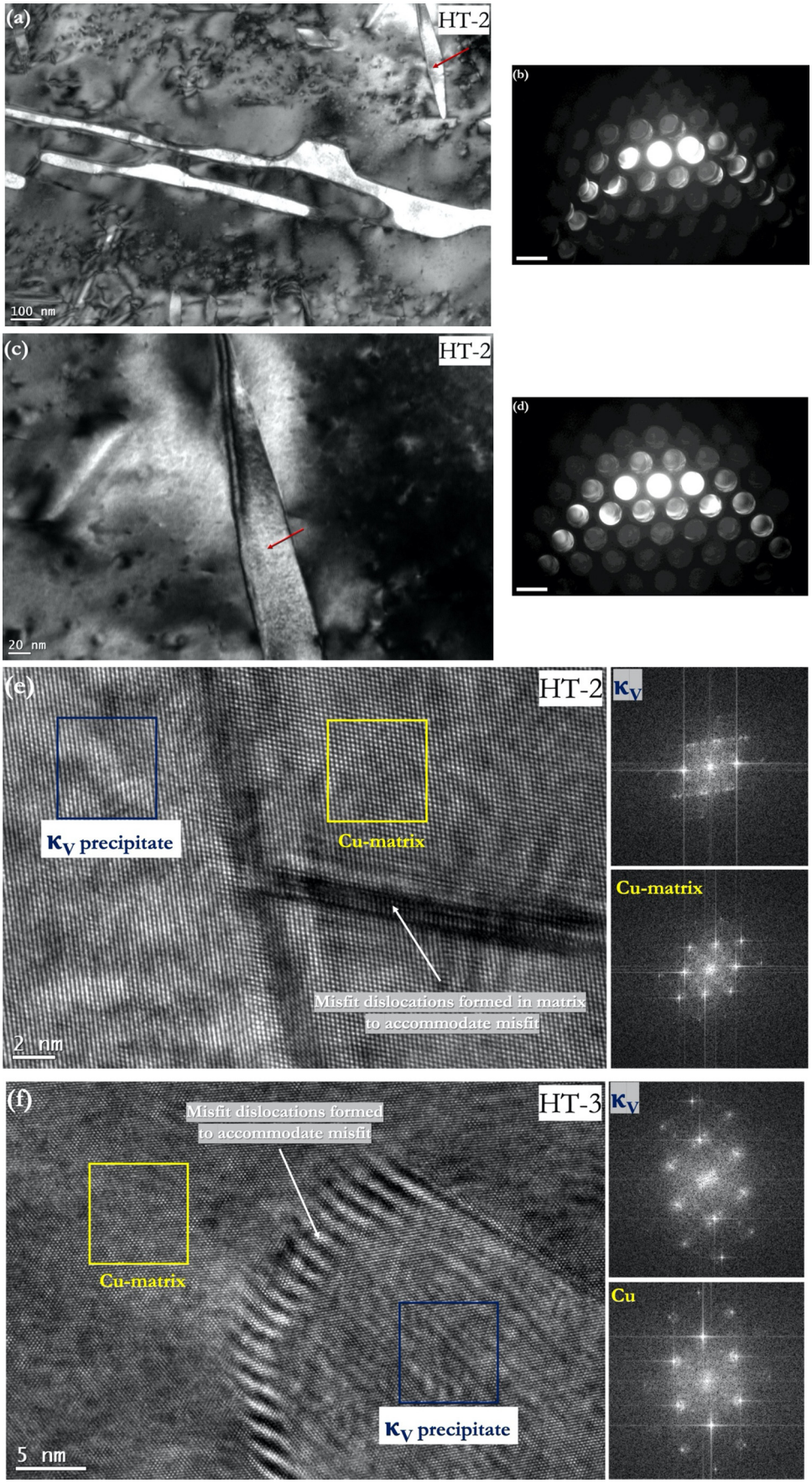

Fig. 11. TEM-Bright field micrographs are showing (a) Cu-matrix and corresponding (b) CBED pattern taken at [110] zone axis, (c) needle-like κ_V precipitate (shown by red arrows) and its corresponding (d) CBED diffraction pattern. HRTEM images of κ_V precipitate in (e) HT-2 and (f) HT-3 samples along with the corresponding FFT patterns of κ_V and α-matrix.

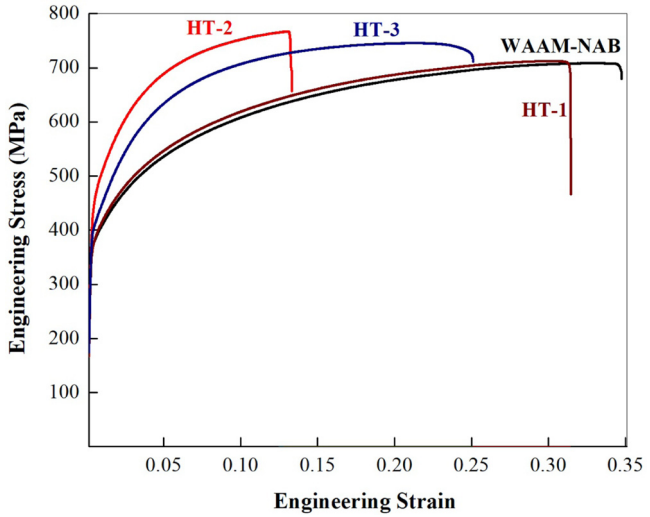

Fig. 12. Typical tensile stress-strain plots of WAAM-NAB samples in as-fabricated and heat-treated conditions.

Table 3
Tensile test results (with standard deviation) of NAB for WAAM and HT samples.

Material	0.2 % Offset Yield Strength (MPa)	Ultimate tensile strength (MPa)	% Elongation
WAAM (As-built)	380 ± 9	708 ± 8	34 ± 1
HT-1	380 ± 12	710 ± 7	32 ± 2
HT-2	471 ± 8	767 ± 10	14 ± 1
HT-3	413 ± 14	745 ± 8	28 ± 1

samples. These results are consistent with several previous reports [10,20,29–34] in both casting and welding literature on NAB. Based on the current findings, it appears that stress-relieving of WAAM-NAB samples can be safely carried out at 350 °C without any concerns about unintended microstructural changes. It is known that, stress-relieving can help maximize the stress-corrosion cracking performance in nickel aluminum bronze [10,19,35,36]. The stress-relieving of WAAM-NAB samples can also help minimize dimensional changes and distortion problems during finish machining operations. The effectiveness of the heat treatment at 350 °C in terms of residual stress relief needs to be investigated in future work. Similarly, it is necessary to investigate any impact of the stress-relieving treatment at 350 °C on the general corrosion behavior of WAAM-NAB samples.

As can be expected, heat-treatment of WAAM-NAB samples at 550 °C for 4 h has resulted in noticeable coarsening of globular κ_{II} precipitates. Further, the heat-treatment has caused some breakdown or spheroidization of the lamellar κ_{III} precipitates into globular particles. Spheroidization of the lamellar κ_{III} is known to be beneficial for the corrosion resistance of nickel aluminum bronze [10,16,37–40]. It may be noted that, the heat-treatment at 550 °C does not facilitate any spheroidization of the lamellar κ_{III} precipitates in conventional sand castings as, because of the slower cooling rates, eutectoid decomposition of β-phase into $\alpha + \kappa_{III}$ takes place at higher temperature leading to coarser and thicker κ_{III} lamella. In the case of WAAM-NAB samples, faster cooling rates culminate into finer and thinner κ_{III} lamella. As a result, they tend to spheroidize at a lower temperature and in lesser time.

Another significant effect of the heat treatment at 550 °C is the precipitation of numerous very fine needle-like κ_v precipitates within the α-dendrites. As shown in Table 2, κ_v precipitates contain a substantial amount of aluminum, nickel, and iron. It is expected that the fine, spherical intradendritic κ_{IV} precipitates initially present in the as-fabricated samples undergo complete dissolution on heating to 550 °C. As a consequence, Fe and Ni contents in the α-solid solution would increase beyond the solubility limits leading to the formation of needle-like κ_v precipitates at 550 °C. The extent of needle-like κ_v precipitation would be governed by the solubility limits of Fe and Ni in α-solid solution at the heat treatment temperature. Subsequently, on cooling from 550 °C to room temperature, reduced solubilities for Fe and Ni would trigger fresh precipitation of fine spherical κ_{IV} particles in the α-matrix. This hypothesis of the dissolution of κ_{IV} precipitates on heating and re-precipitation of the same on cooling is supported by the observation that the size of κ_{IV} precipitates in HT-2 samples did not increase much as compared to the as-fabricated samples. The reduction in the amount of intradendritic κ_{IV} precipitates in HT-2 samples is due to the precipitation of needle-like κ_v precipitates at the heat-treatment temperature (hence, reduced availability of Fe on-cooling for κ_{IV} precipitation).

The significant increase in strength and decrease in ductility after heat treatment at 550 °C for 4 h can be attributed to extensive precipitation of needle-like κ_v in the α-dendrites. It is expected that, the increase in the time of heat treatment at 550 °C may have still caused more pronounced precipitation of needle-like κ_v precipitates affecting the tensile ductility further. While the gain in strength is very attractive, the drop-in ductility may be a concern in heat-treating the WAAM-NAB parts at 550 °C. Further, significant fresh precipitation of needle-like κ_v phases may be detrimental for the corrosion performance of the WAAM-NAB parts. In nickel aluminum bronze, all forms of κ-precipitates have a negative influence on the corrosion resistance. Because of their lamellar morphology (hence, more surface area for galvanic coupling), the κ_{III} precipitates are particularly detrimental. The needle-like κ_v precipitates also present a large surface area for galvanic coupling and can be equally detrimental to the corrosion resistance.

Heat-treatment of WAAM samples at 675 °C for 6 h has resulted in the most amounts of coarsening of the globular κ_{II} precipitates and almost complete spheroidization of the lamellar κ_{III} precipitates. This heat-treatment is known to bring about nearly complete spheroidization of κ_{III} precipitates even in conventional sand castings of nickel aluminum bronze [10]. Spheroidization of κ_{III} lamellae involve a breakdown of each κ_{III} lamella into multiple nearly spherical particles. This is evidenced by the presence of multiple spherical κ-particles in a lined-up manner in the interdendritic regions. As compared to HT-2, heat treatment at 675 °C has resulted in much coarser needle-like κ_v-precipitates in the α-dendrites. This is consistent with the general phenomena that precipitation at higher temperatures tends to be coarser. It appears that heat treatment at 675 °C for 6 h allows for more complete precipitation of needle-like κ_v precipitation as compared to heat-treatment at 550 °C for 4 h. This is supported by the observation that on-cooling κ_{IV} precipitation in HT-3 samples is significantly lesser than in HT-2 samples (note that both HT-2 and HT-3 samples were similarly furnace cooled). In addition, the proportion of iron for the κ_v phase in HT-3 increased (Table 2) as the heat-treatment temperature was raised, which indicates that the Fe-rich κ_{IV} precipitation is taken up by the κ_v phase.

Heat treatment of the WAAM-NAB samples at 650 °C for 6 h seems to provide the best combination of strength and ductility. The increase in strength when compared to the as-fabricated condition is not as striking as in the case of HT-2 for two reasons: i) the presence of coarser and fewer needle-like κ_v precipitates, and ii) reduced amount of fine, spherical intradendritic κ_{IV} precipitation. Similarly, along with the coarser needle-like κ_v precipitation, complete spheroidization of the lamellar κ_{III} precipitates in HT-3 samples is responsible for their superior tensile ductility as compared to HT-2 samples. These microstructural features can also be expected to benefit the corrosion resistance of HT-3 samples.

In summary, from the current findings, heat-treatment of WAAM-NAB parts at 350 °C is most appropriate to consider if the intent is only

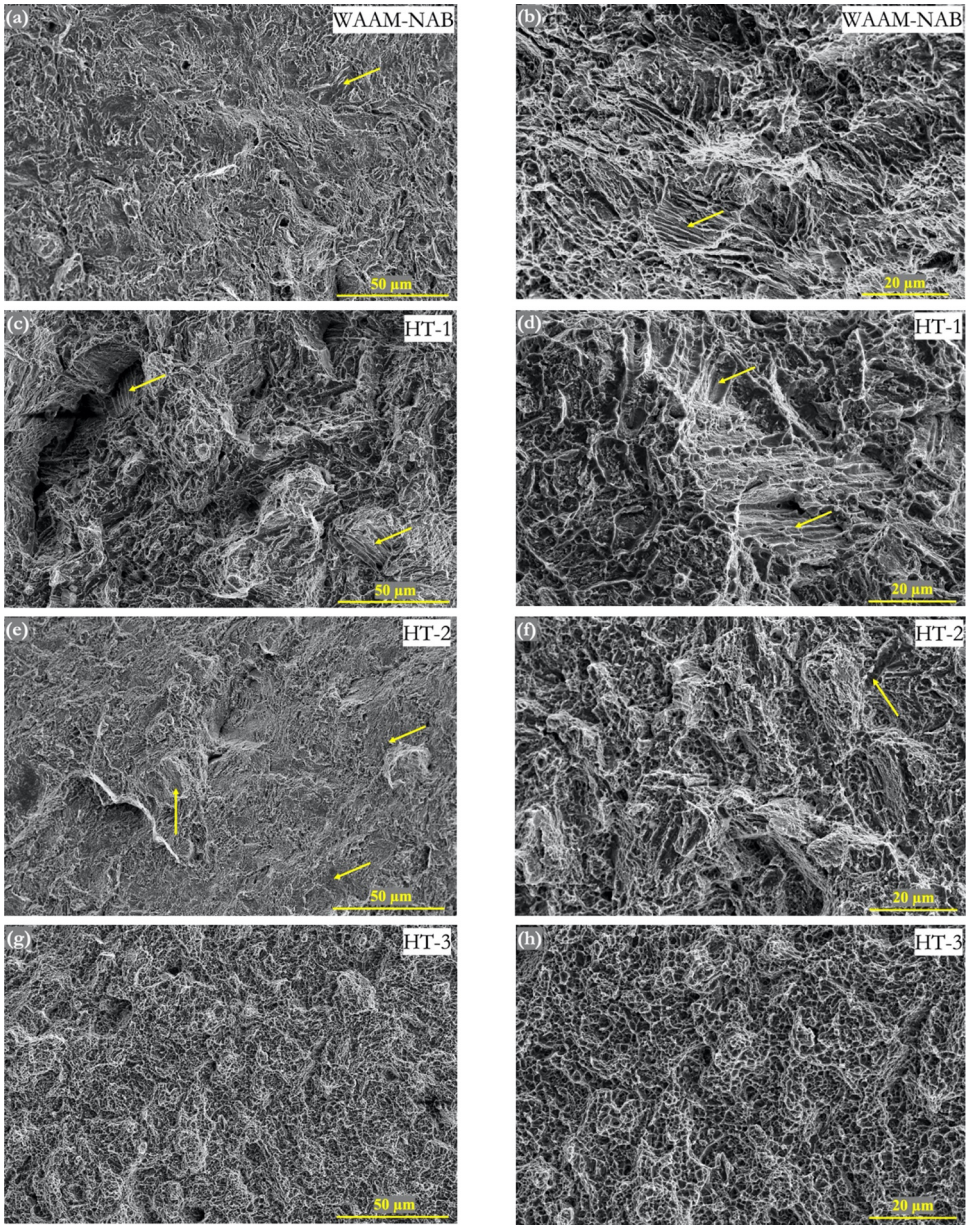

Fig. 13. SEM fractography of as-fabricated (a and b), HT-1 (c and d), HT-2 (e and f), and HT-3 (g and h) tensile specimens. Yellow arrows show local regions of flat fracture surfaces that correspond to lamellar κ_{III} in the interdendritic region. Note that similar features are not observed in HT-3 due to the breakdown of lamellar into globular particles.

stress-relieving. Heat-treatment at 550 °C may be considered for maximizing yield and tensile strength in WAAM-NAB parts if the attendant loss in ductility is acceptable. In applications where a good combination of strength and ductility is called for, heat-treatment at 675 °C may be used. It is essential to consider the corrosion behavior of WAAM-NAB parts after various heat-treatments before arriving at the most appropriate post-processing heat-treatment.

5. Conclusions

This study has aimed to investigate the influence of three different heat-treatment conditions on the microstructural transformations of wire-arc additive manufactured nickel aluminum bronze and correlate mechanical properties along the building direction. The following conclusions are drawn from this study.

(i) Heat-treatment of WAAM-NAB samples at 350 °C for 2 h does not cause any significant microstructural changes. Coarsening of the intradendritic κ_{IV} precipitates is also not a concern. Samples heat-treated at 350 °C exhibit very similar tensile properties as compared to those in as-fabricated condition.

(ii) Heat-treatment of WAAM-NAB samples at 550 °C for 4 h results in extensive needle-like κ_v precipitation in the α-dendrites as well as noticeable coarsening of globular κ_{II} and partial spheroidization of lamellar κ_{III} phases in the interdendritic regions. These samples show some reduction in the amount of intradendritic κ_{IV} precipitation. Samples heat-treated at 550 °C show a significant increase in strength at the expense of tensile ductility as compared to the as-fabricated samples.

(iii) Heat-treatment of WAAM-NAB samples at 675 °C for 6 h causes pronounced coarsening of globular κ_{II} and complete spheroidization of lamellar κ_{III} phases in the interdendritic regions. These samples show much coarser needle-like κ_v precipitates in the α-dendrites as well as considerably reduced amount of intradendritic

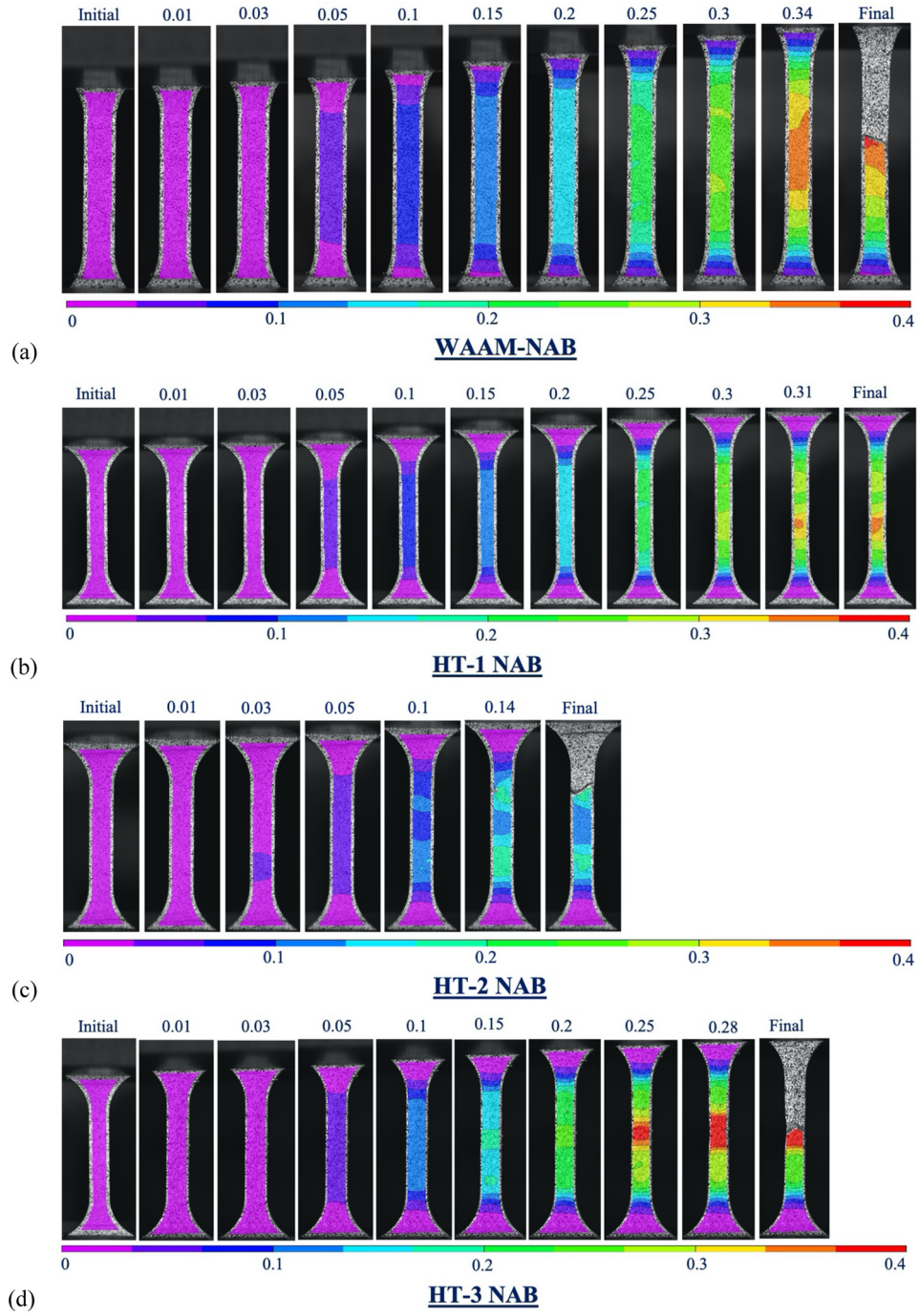

Fig. 14. DIC images of strain-fields during quasi-static tension of (a) WAAM-NAB (as-built), (b) HT-1 NAB, (c) HT-2 NAB, and (d) HT-3 NAB. The build direction is parallel to the tensile axis in all the conditions.

κ_{IV} precipitation. Samples heat-treated at 675 °C showed better strength compared to those in as-fabricated conditions, although the gain is not as striking as that after heat treatment at 550 °C. However, heat treatment at 675 °C does not cause any severe loss of tensile ductility.

CRediT authorship contribution statement

C. Dharmendra: Conceptualization, Investigation, Data curation, Visualization, Validation, Writing - original draft. **B.S. Amirkhiz:** Methodology, Investigation. **A. Lloyd:** Methodology, Investigation. **G.D. Janaki Ram:** Conceptualization, Formal analysis, Writing - review & editing. **M. Mohammadi:** Conceptualization, Supervision, Visualization, Funding acquisition.

Declaration of Competing Interest

The authors report no declarations of interest.

Acknowledgements

The authors would like to thank Natural Sciences and Engineering Research Council of Canada (NSERC) grant number RGPIN-2016-04221, New Brunswick Innovation Foundation (NBIF) grant number

RIF 2018-005, Atlantic Canada Opportunity Agency (ACOA)- Atlantic Innovation Fund (AIF) project number 210414, Mitacs Accelerate Program grant number IT10669 for providing sufficient funding to execute this work. The authors would like to acknowledge Alexander Riemann of Gefertec GmbH for fabricating the nickel aluminum bronze via wire-arc additive manufacturing technique, Dr. Douglas Hall and Steven Cogswell at UNB's Microscopy and Microanalysis Facility for SEM, and Pei Liu and Catherine Bibby at CanmetMATERIALS for TEM sample preparations.

References

[1] T. Debroy, H.L. Wei, J.S. Zuback, T. Mukherjee, J.W. Elmer, J.O. Milewski, A.M. Beese, A. Wilson-Heid, A. De, W. Zhang, Additive manufacturing of metallic components – process, structure and properties, Prog. Mater. Sci. 92 (2018) 112–224, https://doi.org/10.1016/j.pmatsci.2017.10.001.

[2] A. Shahriari, L. Khaksar, A. Nasiri, A. Hadadzadeh, B.S. Amirkhiz, M. Mohammadi, Microstructure and corrosion behavior of a novel additively manufactured maraging stainless steel, Electrochim. Acta 339 (2020) 135925, https://doi.org/10.1016/j.electacta.2020.135925.

[3] D. Herzog, V. Seyda, E. Wycisk, C. Emmelmann, Additive manufacturing of metals, Acta Mater. 117 (2016) 371–392, https://doi.org/10.1016/j.actamat.2016.07.019.

[4] W.E. Frazier, Metal additive manufacturing: a review, J. Mater. Eng. Perform. 23 (2014) 1917–1928, https://doi.org/10.1007/s11665-014-0958-z.

[5] C. Dharmendra, A. Hadadzadeh, B.S. Amirkhiz, A. Lloyd, M. Mohammadi, Deformation Mechanisms and fracture of electron beam melted Ti-6Al-4V, Mater. Sci. Eng. A 771 (2020) 138652, https://doi.org/10.1016/j.msea.2019.138652.

[6] C. Powell, H. Stillman, Corrosion Behavior of Copper Alloys Used in Marine Aquaculture, International Copper Association, Ltd., Madison, New York, 2009.

[7] E.A. Culpan, A.G. Foley, The detection of selective phase corrosion in cast nickel aluminum bronze by acoustic emission techniques, J. Mater. Sci. 17 (1982) 953–964, https://doi.org/10.1007/BF00543513.

[8] V.A. Callcut, Aluminium bronze for industrial use, Met. Mater. 5 (3) (1989) 128–132.

[9] E.A. Culpan, G. Rose, Microstructural characterization of cast nickel aluminium bronze, J. Mater. Sci. 13 (1978) 1647–1657, https://doi.org/10.1007/BF00548728.

[10] I. Richardson, Guide to Nickel Aluminum Bronze for Engineers, Copper Development Association Publication, Helmel Hempstead, 2016.

[11] J.R. Davis (Ed.), Copper and Copper Alloys, ASM Specialty Handbook, ASM International, Materials Park, Ohio, USA, 2001.

[12] C. Dharmendra, A. Hadadzadeh, B.S. Amirkhiz, G.D. Janaki Ram, M. Mohammadi, Microstructural evolution and mechanical behavior of nickel aluminum bronze Cu-9Al04Fe-4Ni-1Mn fabricated through wire-arc additive manufacturing, Addit. Manuf. 30 (2019) 100872, https://doi.org/10.1016/j.addma.2019.100872.

[13] T. Murray, S. Thomas, Y. Wu, W. Neil, C. Hutchinson, Selective laser melting of nickel aluminum bronze, Addit. Manuf. 33 (2020) 101122, https://doi.org/10.1016/j.addma.2020.101122.

[14] C.J. Barr, D.T. McDonald, K. Xia, Significantly enhanced tensile strength and ductility in nickel aluminum bronze by equal channel angular pressing and subsequent heat treatment, J. Mater. Sci. 48 (2013) 4749–4757, https://doi.org/10.1016/j.addma.2020.101122.

[15] Aluminium Bronze Alloys – Corrosion Resistance Guide, Copper Development Association, 1981 Publication No. 80.

[16] E.A. Culpan, G. Rose, Corrosion behavior of cast nickel aluminum bronze in sea water, Br. Corros. J. 14 (3) (1979) 160–166, https://doi.org/10.1179/000705979798275681.

[17] Y. Ding, Y. Lv, B. Zhao, Y. Han, L. Wang, W. Lu, Response relationship between loading condition and corrosion fatigue behavior of nickel-aluminum bronze alloy and its crack tip damage mechanism, Mater. Charact. 144 (2018) 356–367, https://doi.org/10.1016/j.matchar.2018.07.033.

[18] Z. Wu, Y.F. Cheng, L. Liu, W. Lv, W. Hu, Effect of heat treatment on microstructure evolution and erosion-corrosion behavior of a nickel-aluminum bronze alloy in chrolide solution, Corros. Sci. 98 (2015) 260–270, https://doi.org/10.1016/j.corsci.2015.05.037.

[19] Y. Ding, Y. Lv, K. Chen, B. Zhao, Y. Han, L. Wang, W. Lu, Effects of microstructure on the stress corrosion cracking behavior of nickel-aluminum bronze alloy in 3.5% NaCl solution, Mater. Sci. Eng. A 733 (2018) 361–373, https://doi.org/10.1016/j.msea.2018.07.066.

[20] M.D. Fuller, S. Swaminathan, A.P. Zhilyaev, T.R. McNelley, Microstructural transformations and mechanical properties of cast NiAl bronze: effects of fusion welding and friction stir processing, Mater. Sci. Eng. A 463 (2007) 128–137, https://doi.org/10.1016/j.msea.2006.07.157.

[21] C. Shen, Z. Pan, D. Ding, L. Yuan, N. Nie, Y. Wang, D. Luo, D. Cuiuri, S.V. Duin, H. Li, The influence of post-production heat treatment on the multi-directional properties of nickel-aluminum bronze alloy fabricated using wire-arc additive manufacturing process, Addit. Manuf. 23 (2018) 411–421, https://doi.org/10.1016/j.addma.2018.08.008.

[22] C. Shen, G. Mu, X. Hua, F. Li, D. Luo, X. Ji, C. Zhang, Influences of postproduction heat treatments on the material anisotropy of nickel-aluminum bronze fabricated using wire-arc additive manufacturing process, Int. J. Adv. Manuf. Technol. 103 (2009) 3199–3209, https://doi.org/10.1007/s00170-019-03700-7.

[23] E8/E8M-15a Standard Test Methods for Tension Testing of Metallic Materials, ASTM, 2015.

[24] C. Dharmendra, S. Shakerin, G.D. Janaki Ram, M. Mohammadi, Wire-arc additive manufacturing of nickel aluminum bronze/stainless steel hybrid parts – interfacial characterization, prospects, and problems, Materialia (2020) 100834, https://doi.org/10.1016/j.mtla.2020.100834.

[25] N.K. Sharma, S. Shekhar, Cut-off deviation for CSL boundaries in recrystallized face-centered cubic materials, Philos. Mag. 97 (2017) 2004–2017, https://doi.org/10.1080/14786435.2017.1322730.

[26] M. Cook, W.P. Fentiman, E. Davis, Observations on the structure and properties of wrought copper-aluminium-nickel-iron alloys, J. Inst. Met. 80 (1952) 419–429.

[27] D.M. Lloyd, G.W. Lorimer, N. Ridley, Characterization of phases in a nickel-aluminium bronze, Met. Technol. 7 (1980) 114–119, https://doi.org/10.1179/030716980803286577.

[28] F. Hasan, A. Jahanafrooz, G.W. Lorimer, N. Ridley, The morphology, crystallography, and chemistry of phases in as-cast nickel-aluminum bronze, Metall. Trans. 13A (1982) 1337–1345, https://doi.org/10.1007/BF02642870.

[29] A. Jahanafrooz, F. Hasan, G.W. Lorimer, N. Ridley, Microstructural development in complex nickel-aluminum bronzes, Metall. Trans. A 14A (1983) 1951–1956, https://doi.org/10.1007/BF02662362.

[30] F. Hasan, G.W. Lorimer, N. Ridley, Tempering of cast nickel-aluminum bronze, Met. Sci. 17 (1983) 289–296, https://doi.org/10.1179/030634583790420826.

[31] Welding of Aluminum Bronzes, Copper Development Association, 1988 Publication No. 85.

[32] S.K. Menon, F.A. Pierce, B.P. Rosemark, K. Oh-Ishi, S. Swaminathan, T.R. McNelley, Strengthening mechanisms in NiAl bronze: hot deformation by rolling and friction stir processing, Metall. Mater. Trans. A 43 (2012) 3687–3702, https://doi.org/10.1007/s11661-012-1181-x.

[33] Z. Wu, Y.F. Cheng, L. Liu, W.J. Lv, W.B. Hu, Effect of heat treatment on microstructure evolution and erosion-corrosion behavior of a nickel-aluminum bronze alloy in chloride solution, Corros. Sci. 98 (2015) 260–270, https://doi.org/10.1016/j.corsci.2015.05.037.

[34] C.V. Hyatt, K.H. Magee, T. Betancourt, The effect of heat input on the microstructure and properties of nickel aluminum bronze laser clad with a consumable of composition Cu-9.0Al-4.6Ni-3.9Fe-1.2Mn, Metall. Mater. Trans. A 29A (1998) 1677–1690, https://doi.org/10.1007/s11661-998-0090-5.

[35] H.T. Michels, R.M. Kain, Effect of Composition and Microstructure on the Seawater Corrosion Resistance of Nickel-Aluminum Bronze, Paper No. 03262, NACE Corrosion NACE International, Houston, Texas, 2003.

[36] Z. Wu, Y.F. Cheng, L. Liu, W.J. Lv, W.B. Hu, Effect of heat treatment on microstructure evolution and erosion-corrosion behavior of a nickel-aluminum bronze alloy in chloride solution, Corros. Sci. 98 (2015) 260–270, https://doi.org/10.1016/j.corsci.2015.05.037.

[37] F. Yang, H. Kang, E. Guo, R. Li, Z. Chen, Y. Zeng, T. Wang, The role of nickel in mechanical performance and corrosion behavior of nickel-aluminum bronze in 35 wt.% NaCl solution, Corros. Sci. 139 (2018) 333–345, https://doi.org/10.1016/j.corsci.2018.05.012.

[38] J.A. Wharton, R.C. Barik, G. Kear, R.J.K. Wood, K.R. Stokes, F.C. Walsh, The corrosion of nickel-aluminum bronze in sea water, Corros. Sci. 47 (2005) 3336–3367, https://doi.org/10.1016/j.corsci.2005.05.053.

[39] G.W. Lorimer, F. Hasan, J. Iqbal, N. Ridley, Observation of microstructure and corrosion behavior of some aluminium bronzes, Br. Corros. J. 21 (1986) 244–248, https://doi.org/10.1179/000705986798272046.

[40] Y. Sun, H. Wang, W. Liu, G. Song, Q. Li, Improvement of surface resistance to cavitation corrosion of nickel aluminum bronze by electropulsing-assisted ultrasonic surface rolling process, Surf. Coat. Technol. 368 (2019) 215–223, https://doi.org/10.1016/j.surfcoat.2019.03.045.